Digest Journal of Nanomaterials and Biostructures Vol. 20, No. 2, April - June 2025, p. 669 - 679

Investigating the effects of Hg doping on WO_3 nanoflakes: a hydrothermal route to tailored properties

S. Saranya, L. Balakrishnan *, D. Sangeetha, S. Lakshmi Priya
Department of Physics, Government College of Technology, Coimbatore 641 013, Tamil Nadu, India

This study employed hydrothermal technique to synthesize tungsten oxide (WO_3) and mercury doped WO_3 (Hg:WO_3) nanoparticles (NPs). X-ray diffraction results confirmed the monoclinic phase of all NPs. Field emission scanning electron microscopy verified the nanoflake morphology, while energy dispersive X-ray analysis and X-ray photoelectron spectroscopy confirmed the presence and +2 oxidization state of Hg in doped NPs. Raman spectroscopy provided insights into the chemical structure and phase crystallinity. The optical properties were improved by Hg doping, as evident from ultraviolet-visible diffuse reflectance spectroscopy which showed enhanced visible-light absorption. The bandgap of WO_3 reduced from 2.84 to 2.57 eV after Hg doping. The photoluminescence spectroscopy shows decreased emission peak intensity for Hg:WO_3. These results indicate that Hg:WO_3 NPs are suitable for visible light-driven applications.

(Received February 18, 2025; Accepted June 18, 2025)

Keywords: Tungsten oxide, Bandgap, doping, Nanoflakes, Mercury doped WO_3

1. Introduction

Tungsten oxide (WO_3) has gathered substantial scientific attention in recent periods due to its exclusive and fascinating properties. As a noteworthy transition metal oxide semiconductor, the bandgap energy of WO_3 ranges from 2.8-3.1 eV [1] and exhibits various crystallographic phases including monoclinic, orthorhombic hexagonal and cubic structures at different thermal treatments [2]. Owing to its properties such as non-toxicity, economic feasibility and optical characteristics, make it a perfect material for different applications including smart windows, sensors, electrochromic, photocatalyst and photodetectors [3, 4]. Its ability to assist effectual charge carrier separation, chemical stability and high carrier mobility strengthens its suitability for these applications [5]. Furthermore, in WO_3 crystal structure, W^{6+} is bonded to six O^{2-} atoms to form distorted corner-sharing WO_6 octahedral which allows for easy doping and modification, aiding tailored properties for specific usages [6].

The photoresponsive behavior, tunable structure and constant ratio formation of WO_3, have flashed considerable attention. However, its limited response to the blue and near-ultraviolet regions of the solar range obstructs its potential. To overcome this, narrowing the bandgap through doping/alloying with appropriate element has become a main objective. By introducing dopant elements, the bandgap of WO_3 can be effectually reduced without conceding structural properties [7]. Several methods have been hired to synthesize doped transition metal oxide nanoparticles (NPs) including hydrothermal [8], colloidal chemical, RF thermal plasma [9], sol-gel [10] and chemical co-precipitation [11]. Among these, the hydrothermal technique stands out as a useful and environmentally approachable method for preparing WO_3 NPs [12]. The rare earth materials associated with high price, limited accessibility and environmental outlet doping WO_3 with low-cost, abundant and environmentally reliable metal ions are essential [3]. Although this extensive research on doping WO_3 with such metal ions remains unusual.

Optimization of semiconductor properties through doping has been widely researched. Similarly, doping TiO_2 with numerous elements such as Cu [13, 14], Al/N [15], Cu/S [16] and Cu/N [17] has improved its visible optical performance. This material doping shows higher optical properties compared to pure TiO_2, explaining the doping potential to tailor TiO_2 optical performance

* Corresponding author: bslv85@gmail.com
https://doi.org/10.15251/DJNB.2025.202.669

for specific uses. Moreover, research has exposed that doping ZnO with Cd [18], significantly improves its photoresponsiveness in the visible range, compared to pure ZnO. In the same approach, WO_3 doped with transition metals such as Ta [19], Fe [20], Mg [21] Ag [22], Zn [18], Cu [23] and Cd [24], reveals increased visible light absorption, accomplish it an effectually visible-light-induced photodetector and photocatalyst [25].

Despite extensive study on WO_3 doping, a vital knowledge gap continues regarding the tuning of its bandgap by mercury (Hg) doping. Stating this, the present research synthesizes Hg-doped WO_3 (Hg:WO_3) NPs via hydrothermal method, exploring the unknown territory of Hg doping in WO_3. This search aims to explicate the profound influence of Hg doping on the structural, morphological, optical and elemental properties of WO_3 NPs. Furthermore, the optical properties including absorption, reflection and photoluminescence are examined to unravel the changes induced by Hg doping. The elemental composition and chemical states are also studied to determine the incorporation of Hg into the WO_3 lattice. The findings of this research will provide critical perceptions into the changes induced by Hg doping, necessary for tailoring WO_3 NPs properties for various applications. Specifically, the tailored bandgap and enhanced optical conductivity of Hg:WO_3 NPs are predicted to improve photodetectivity and photocatalytic activity.

This research aims to assist the visible region properties of WO_3 by widening the band gap and thereby enhancing the absorption in the visible region by doping/alloying with Hg.

2. Experimental analysis

2.1. Sample preparation

Sodium tungstate dihydrated ($Na_2WO_4.2H_2O$, 97%), mercury nitrate monohydrate ($(Hg(NO_3)_2).H_2O$, 98%) precursors used were purchased from Sigma-Aldrich. Deionized (DI) water was used as the solvent and Cetyltrimethylammonium bromide (CTAB) ($C_{16}H_{33}N(CH_3)_3Br$) was hired as a capping agent. Hydrochloric acid (HCl) was used as a precipitating agent.

2.2. Synthesis

WO_3 and Hg:WO_3 NPs were synthesized via a hydrothermal method. Initially, 7 g of $Na_2WO_4 \cdot 2H_2O$ were dissolved in 75 mL of DI water to form a clear solution. Then, 0.05 g of CTAB dissolved in 20 mL of DI water were added to the dissolved solution. The above solution was continuously stirred for about 1 h. HCl was added dropwise to the solution until the pH reaches 1 which subsequently resulted in a pastel yellow colored precipitate. The precipitate was then filled to a 200 mL Teflon-coated autoclave and it was tightly sealed and exposed to a hydrothermal setup at a temperature of 130 °C for about 24 h. After the hydrothermal reaction, the resultant yellow precipitate was separated from the solution via centrifugation process. The precipitate was then washed alternatively with DI water and ethanol in order to remove any impurities. Later, the washed precipitate was dried at 80 °C in an oven for 7 h. The dried precipitate was then hand grinded for about 30 minutes to make a fine powder. Finally, the obtained powder was annealed in a muffle furnace at a temperature of 500 °C for about 2 h to get yellow colored pure WO_3 NPs.

2.2.1. Synthesis of Hg doped WO_3 NPs

The synthesis of mercury-doped WO_3 (Hg:WO_3) NPs followed the same procedure as pure WO_3, with dopant concentration variation (5-20 at. %) as shown in fig. 1. Hg $(NO_3)_2).H_2O$ served as precursors for Hg dopants, for 5 at. % Hg:WO_3 NPs, Hg $(NO_3)_2$. H_2O (0.340 g) was dissolved thoroughly in 50 ml of DI water. It is then added to the precursor solution after adding CTAB. The subsequent steps mirrored the pure WO_3 synthesis procedure. The schematic representation are shown in Figure 1.

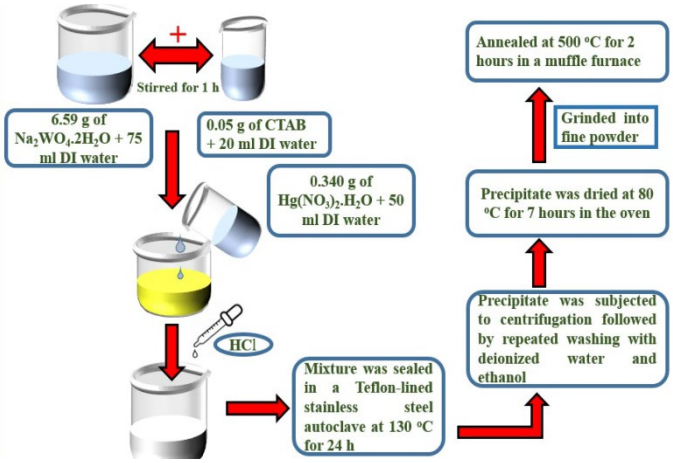

Fig. 1. Schematic illustration of hydrothermal method of Hg doped WO_3 NPs.

2.3. Characterization techniques

The synthesized WO_3 and Hg:WO_3 NPs were further analyzed using different techniques to examine their structural, morphological, optical, and elemental properties in detail. X-ray diffraction (XRD) peaks were analyzed using an X'pert PRO powder X-ray diffractometer with Cu-Kα radiation (λ = 1.54178 Å) to study the crystal structure. Field emission scanning electron microscopy (FE-SEM) with energy dispersive X-ray analysis (EDAX) was analyzed using an FEI Quanta – 250 to examine the surface morphology and elemental distribution. UV-Visible diffuse reflectance spectrometry (DRS) spectra were analyzed on a Thermofisher Evolution 220 spectrophotometer to study the optical behavior. A PeakSeeker Pro-532 Raman spectrometer was used to obtain Raman spectra to investigate vibrational properties. Photoluminescence (PL) spectra were recorded on a Cary Eclipse G9800 Agilent Technologies fluorescence spectrometer to study emission properties. X-ray photoelectron spectroscopy (XPS) was made using Shimadzu ESCA 3400 spectrometer to evaluate the chemical composition.

3. Result and discussion

3.1. Structural analysis

XRD analysis identified the crystallite structure and phase of synthesized WO_3 NPs [3]. In fig. 2a and b show XRD spectra with concentration variation (5-20 at. %) of Hg:WO_3 NPs. The XRD spectra show prominent diffraction peaks, particularly at 2θ values of 23.1°, 23.7° and 24.3°. These peaks agree to the (002), (020) and (200) crystallographic planes, respectively. The presence of these peaks specifies that the NPs show desired growth orientations. This analysis confirms that the prepared NPs crystallizes in the monoclinic symmetry, belonging to the space group P 21/n group no. 14. The lattice parameters, α = 90°, β = 90.9° and γ = 90°, are in agreement with the standard reference pattern (JCPDS card No. 83-0950). This confirms that the perceived crystal structure is consistent with the predictable monoclinic phase of WO_3 [26]. No phase transformation occurred upon doping, indicating phase purity. By using the Cauchy Lorentzian formula specified in equation 1, the crystallite size and strain were calculated and from equation (2) lattice parameters were determined. The results are presented in Table 1,

$$\beta' \cos\theta = \frac{C\lambda}{D} + 4\varepsilon \sin\theta \tag{1}$$

$$\frac{1}{d_{hkl}^2} = \frac{1}{\sin^2\beta}\left[\frac{h^2}{a^2} + \frac{k^2\sin^2\beta}{b^2} + \frac{l^2}{c^2} - \frac{2hl\cos\beta}{ac}\right] \tag{2}$$

This equation let to the formulation of crystallite size (D) and strain (ε) from the FWHM (β') of the diffraction peaks and the diffraction angle (θ). The shape factor (C) and X-ray wavelength (λ) are constants and phase angle (β) [4]. Williamson-Hall (W-H) plots (fig. 3) estimated crystallite size and strain. The XRD patterns reveal characteristic peak shifts due to Hg^{2+} (ionic radius 0.102 nm) substituting W^{6+} (ionic radius 0.060 nm) ions. The large ionic radius of Hg^{2+} causes deviations in d-spacing values, promoting the elevated growth of nanoflakes (NFs) in Hg-doped NPs [27]. Oxygen vacancies in metal oxides alter the O-W-O bond length and lattice parameters leading to changes in optical properties. [3].

Table 1. Calculated crystallographic parameters of pure and Hg:WO_3 NPs at various concentrations.

Compounds		Crystallite Size (D) nm	Strain (ε)	Lattice parameters Å		
				a	b	c
Pure		58.48	0.00178	7.31	7.53	7.69
Hg:WO_3 at. %	5	55.88	0.00247	7.71	7.51	7.35
	10	54.35	0.00158	7.74	7.53	7.37
	15	47.79	0.00182	7.70	7.49	7.34
	20	40.76	0.00154	7.65	7.49	7.30

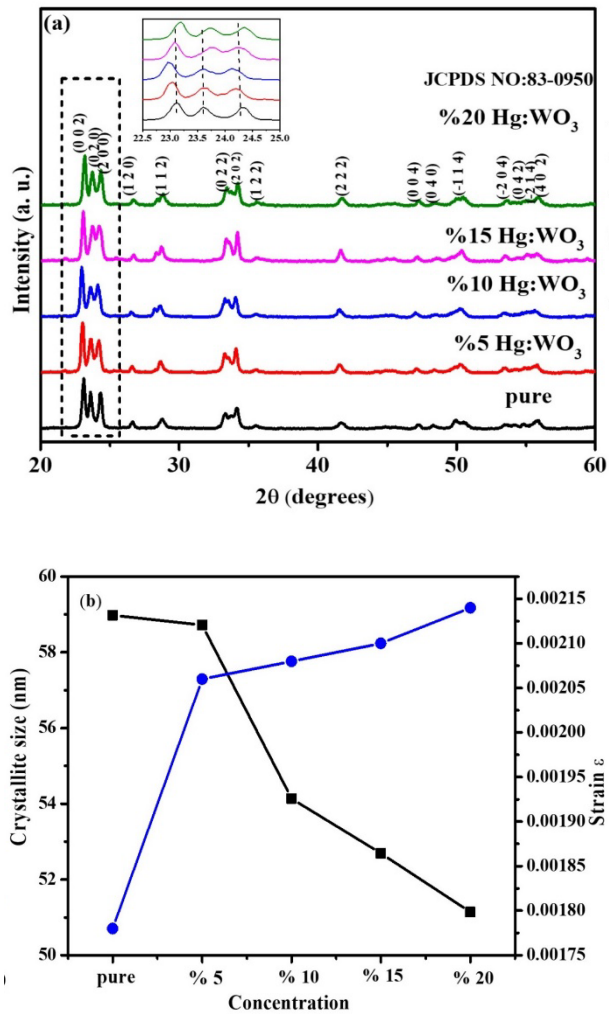

Fig. 2. a) XRD pattern and b) variation of crystallite size with strain of pure WO_3 and Hg:WO_3 NFs.

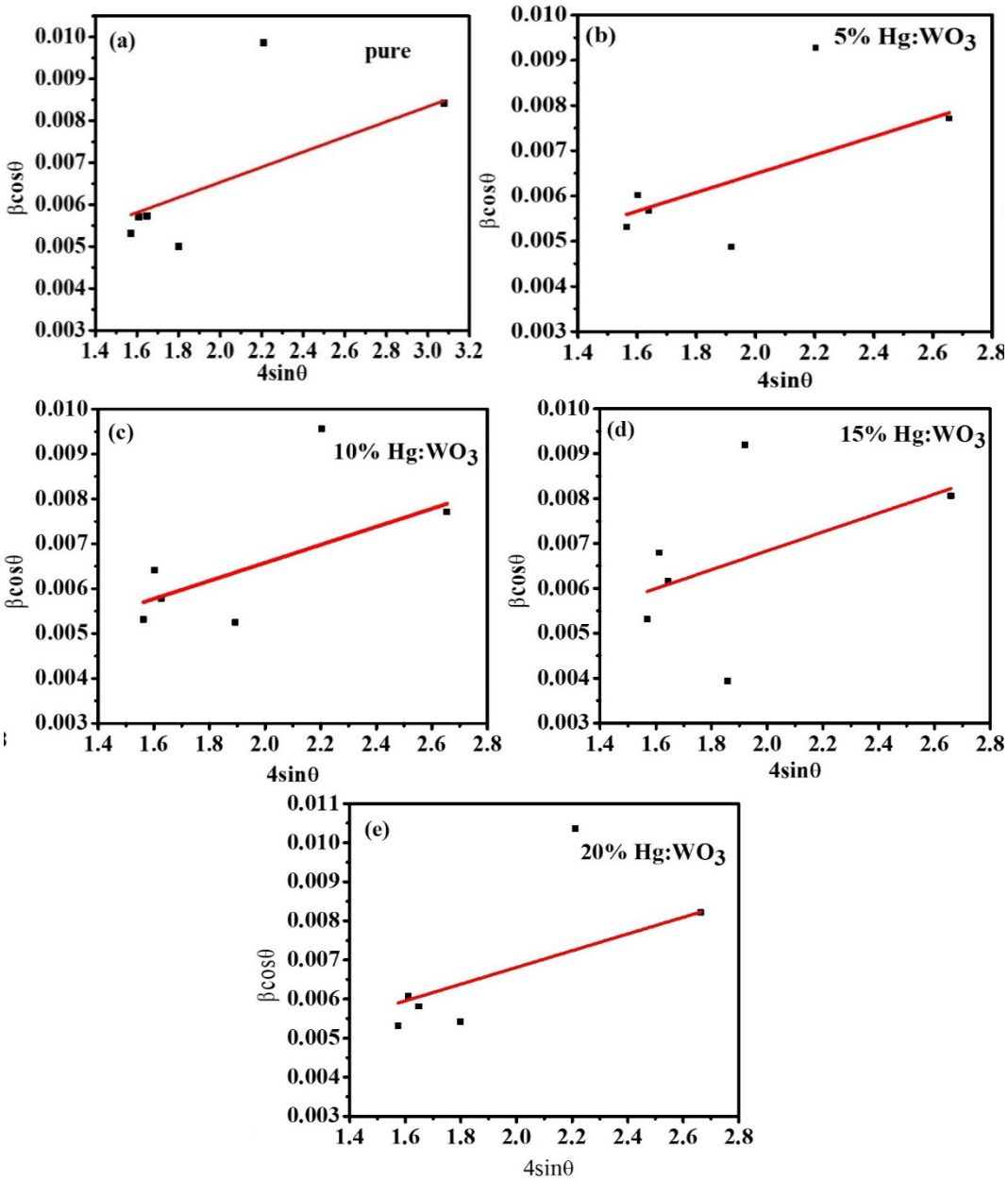

Fig. 3. W-H plot of pure and Hg:WO_3 NFs.

3.2. Morphology

FESEM analysis of Hg:WO_3 NPs is presented in fig. 4a and b. The resolution images were captured at a low scale of 200 nm, with a very high magnification of 50.00 K X, exhibit flake-like morphology for both pure and doped WO_3 NPs. The average size of the NPs decreased from 117 nm for pure WO_3 to 85 nm for Hg:WO_3 NPs, indicating a significant impact of Hg doping on the morphology of WO_3. This observation aligns with previously reported work [28, 29]. EDAX results, shown in fig. 4c and d, confirm the existence of tungsten (W) and oxygen (O) in both pure and doped samples. Additionally, the EDAX spectrum of Hg:WO_3 NPs exhibits distinct peak corresponding to mercury (Hg), verifying successful incorporation of Hg into the WO_3 lattice site.

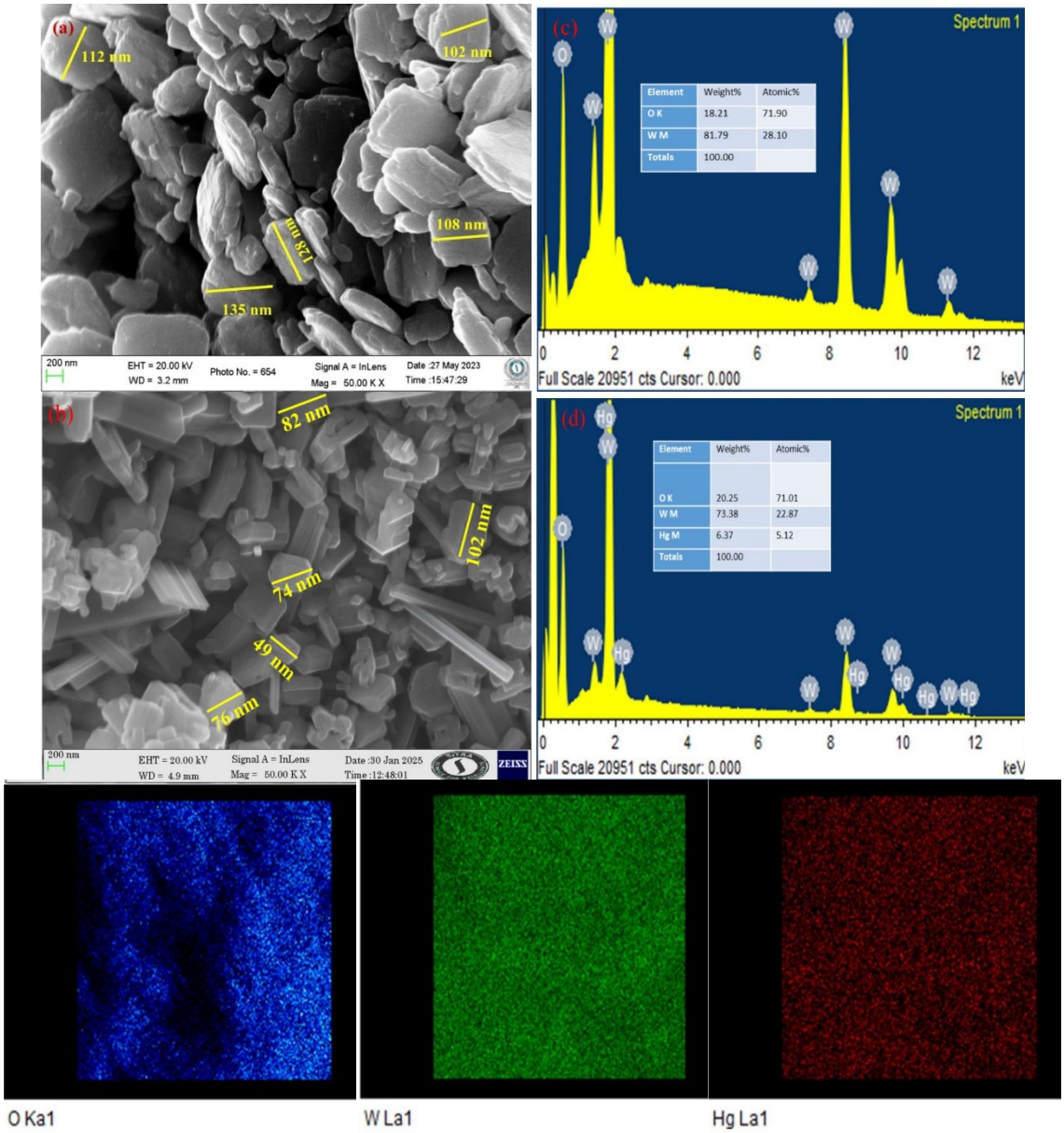

Fig. 4. FESEM of a) pure, b) 20 at. % Hg:WO_3 NFs and EDAX of c) pure, d) 20 at. % Hg:WO_3 NFs and (insert) elemental mapping of O, W and Hg respectively.

3.3. UV-vis (DRS) study

The optical properties of pure and Hg:WO_3 NFs were investigated over a spectral range of 200-1100 nm using UV-vis (DRS) [3]. In fig. 5a present the reflectance (R) and absorbance spectra of pure and Hg:WO_3, showing a substantial reduction in reflectance within the visible region upon incorporation of Hg ions into the WO_3 lattice, representing enhanced visible light absorption. This reflectance decrease is ascribed to improved charge carrier transmission from the valence to the conduction band. Hg doping shifts the absorption towards the visible region, due to the decreased bandgap, making it suitable for visible photodetector application. The Kubelka-Munk method to calculate the bandgap (Eg) of the sample was calculated using the Kubelka-Munk relation,

$$F(R) = \frac{1-R^2}{2R} \tag{3}$$

where the reflectance value (R) is associated with the Kubelka-Munk function F(R). The bandgap energy was estimated through the extrapolation of the linear portion of the $(F(R)\ h\upsilon)^2$ versus $h\upsilon$ curve to the x-axis as shown in fig. 5b. The results show that Hg doping reduces the bandgap of WO_3 from 2.84 eV – 2.57 eV. These values are consistent with previously reported results [3, 4]. Doping WO_3 with metal ions decreases the photo-generated charge carrier recombination rate, attributed to the reduced Eg [30]. Fig. 5c illustrate the optical conductivity (σ_{opt}) versus photon energy, showing enhanced conductivity due to Hg doping. While conductivity remains feeble up to 2.4 eV, it increases significantly from 2.5-3.4 eV.

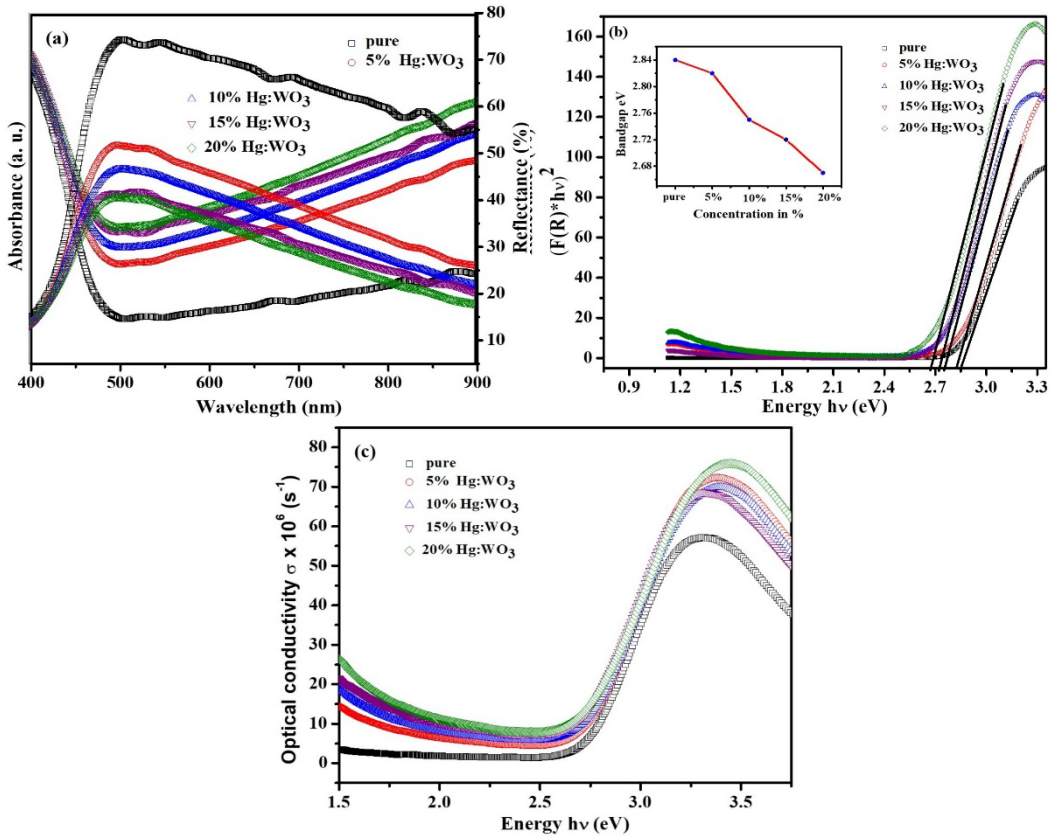

Fig. 5. (a) Reflectance and Absorbance spectra of Hg:WO_3,
(b) Kubelka-Munk of Hg:WO_3 and c) Optical conductivity of Hg:WO_3 NFs.

3.4. Raman study

The bonding details within the WO_3 and Hg doped WO_3 NFs were provided by Raman spectra and are depicted in fig. 6, provide This spectrum illustrates the characteristic bending and stretching mode of WO_3. In Raman spectra, the successful incorporation of Hg^{2+} ions in the WO_3 lattice, indicate the absence of any additional bands, corresponding to Hg-O vibration. Specifically, the spectra reveal two distinct frequency regions, the lower frequency range of 100-300 cm^{-1}, relate to O-W-O bending modes, and the higher frequency range of 600-900 cm^{-1}, ascribed to O-W-O stretching modes. Within these regions, several notable peaks are observed. A prominent peak at 271 cm^{-1} is attributed to the O-W-O characteristic bending mode, while two additional peaks at 715 cm^{-1} and 803 cm^{-1} are assigned to O-W-O characteristic stretching modes. Furthermore, the presence of Raman active modes at 271, 328, 715 and 803 cm^{-1} at room temperature suggests formation of monoclinic phases. Notably, the Raman spectra of Hg-doped WO_3 NFs exhibit a decrease in intensity with increasing dopant percentage. This decrease is likely attributed to changes in particle size, as reported in previous studies [31].

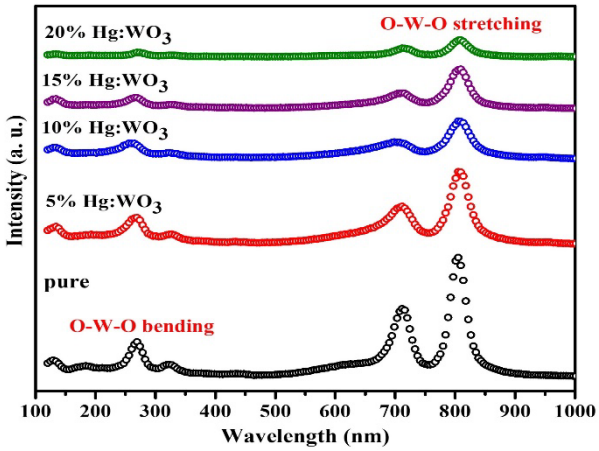

Fig. 6. Raman spectra of pure and Hg:WO_3 NFs.

3.5. Photoluminescence study

PL spectra of pure and Hg:WO_3 NFs, show a emission profile revealing the presence of energy states and various defects within the valence band and conduction bands. The spectra were obtained using a 360 nm excitation wavelength at room temperature exhibited similar characteristics between pure and doped samples as shown in fig. 7. There were no additional spectral features detected in the Hg doped WO_3 samples. The spectra revealed several emission peaks, including 425 nm and 431 nm, attributed to near-band edge transitions and 456 nm, attributed to defect states caused by oxygen vacancies (Vo) [32]. Additionally, peaks at 483 nm, 508 nm and 525 nm were observed, corresponding to defect states due to Hg^{2+} and WO_3 interaction, recombination of electrons to deep defect levels in the WO_3 bandgap, and Vo and tungsten interstitial sites, respectively [33, 34]. The PL spectra of Hg:WO_3 NFs revealed variation in intensity and also, confirming the effective incorporation of Hg^{2+} ions into the WO_3 lattice. The peak intensity decreases while doping of Hg into WO_3 lattice which attributed reduced photoinduced electron-hole pairs recombination rate under visible light irradiation. These findings demonstrate the significant improvement in the optical properties of Hg doped WO_3 NFs [3].

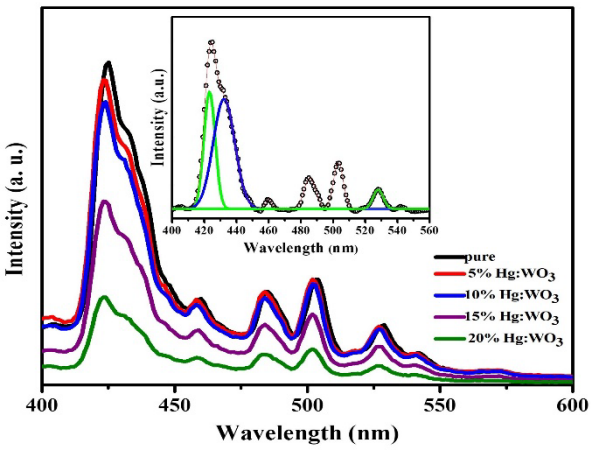

Fig .7. PL spectra of pure and Hg:WO_3 NFs.

3.6. XPS analysis

XPS analysis revealed the oxidation state and elemental composition of pure WO_3 and Hg:WO_3 NFs. The full range scan spectrum showed the presence of W and O peaks in pure WO_3,

while Hg:WO_3 exhibited additional Hg elemental constituents as shown in fig. 8a. Core-level spectra revealed shifts in binding energies, indicating strong bonding between metal ions and oxidation. Specifically, the W 4f peaks shifted to higher binding energies of 0.48 eV and 0.34 eV, suggesting successful incorporation of Hg ions into the W^{6+} ions in the WO_3 lattice fig. 8b. The O1s peak exhibited a lower binding energy of 0.3 eV, indicating that Hg ions increased the oxygen vacancy in the WO_3 lattice as shown in fig. 8c [35]. Furthermore, the Hg 4f core-level spectrum confirmed the incorporation of Hg atoms in Hg^{2+} state, with a binding energy difference of 2.3 eV (fig. 8d). Thereby confirming the presence of divalent mercury ions in the doped WO_3 NFs. These findings demonstrate that Hg ions are effectively integrated into the WO_3 lattice, leading to enhanced absorption in the visible region [36, 37].

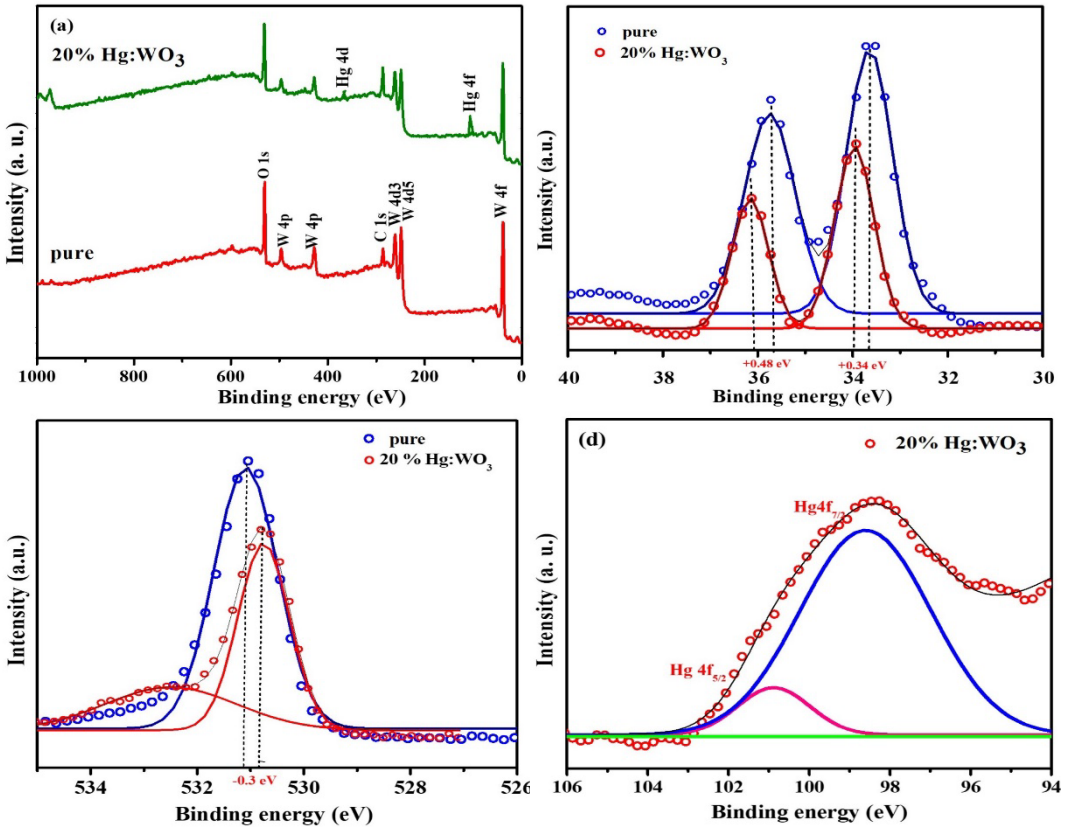

Fig. 8. XPS spectra of (a) Hg:WO_3 NFs, (b) W 4f, (c) O 1s and (d) Hg 4f in WO_3 NFs.

3. Conclusion

In this work, the effect of Hg doping on WO_3 NFs were investigated in detail. WO_3 NFs were synthesized using a hydrothermal technique and successively doped with Hg of various concentrations (5 - 20 at. %). XRD analyzes are indexed to monoclinic symmetry with space group P 21/n. Their morphologies have been observed by FESEM analysis. EDAX and XPS spectra of Hg:WO_3 shown the existence of W, O and Hg and their corresponding oxidation states (W^{6+}, O^2 and Hg^{2+}). The optical reflectance (R) and absorbance spectra of pure and Hg:WO_3, showing a significant decrease in reflectance within the visible region and shifts the absorption towards the visible region. The value of Eg is 2.84 eV and 2.57 eV for pure and 20 at. % Hg doped WO_3 using Kubelka–Munk relation.

The successful incorporation of Hg into WO_3 caused enhanced properties, together with a narrowed Eg. There is a significant enhancement in the visible light absorption making Hg:WO_3 NFs suitable for visible photodetector applications. A suitable photodetector device can be fabricated in the future to investigate the detailed effect of Hg doping on the photodetecting performance of WO_3 NFs.

References

[1] B. Deepa, V. Rajendran, Nano-Structures Nano-Objects 16, 185 (2018); https://doi.org/10.1016/j.nanoso.2018.06.005

[2] E. Spagnoli, S. Krik, B. Fabbri, M. Valt, M. Ardit, A. Gaiardo, L. Vanzetti, M. Della Ciana, V. Cristino, G. Vola, S. Caramori, C. Malagù, V. Guidi, Sensors Actuators: B. Chemical 347, 130593 (2021); https://doi.org/10.1016/j.snb.2021.130593

[3] A.A. Jerold, J.K.S. Mary, C. Joel, R. Biju Bennie, S. Praveen Daniel, Journal of Physics and Chemistry of Solids 157, 110169 (2021); https://doi.org/10.1016/j.jpcs.2021.110169

[4] R. Priya, R. Balan, Journal Environment Nanotechnology 7 (2), 7 (2018); https://doi.org/10.13074/jent.2018.06.182310

[5] C. Fàbrega, S. Murcia-López, D. Monllor-Satoca, JD Prades, MD Hernández-Alonso, G Penelas, JR Morante, T Andreu, Applied catalysis B Environmental 189, 133 (2016); https://doi.org/10.1016/j.apcatb.2016.02.047

[6] J.C. Murillo-Sierra, A. Hernández-Ramírez, L. Hinojosa-Reyes, J.L. Guzmán-Mar, Chemical Engineering Journal Advances 5, 100070 (2021); https://doi.org/10.1016/j.ceja.2020.100070

[7] S. Harini, A. Aswini, S.C. Kale, Jayashri Narawane, Jayant Pawar, Snehal Masurkar, Shilpa Ruikar, International Journal of Current Research and Review 13 (2), 76 (2021); https://doi.org/10.31782/IJCRR.2021.13226

[8] Hamidreza Ahmadian, Fatemeh Shariatmadar Tehrani and Maryam Aliannezhadi, Material Research Express 6, 105024 (2019); https://doi.org/10.1088/2053-1591/ab3826

[9] Haibao Zhang, Mingshui Yao, Liuyang Bai, Fangli Yuan, CrystEngComm 15(7),1432 (2013); https://doi.org/10.1039/c2ce26514a

[10] M. Aliannezhadi, M. Abbaspoor, F. Shariatmadar Tehrani, Mohaddeseh Jamali, Opt Quant Electron 55, 250 (2023); https://doi.org/10.1007/s11082-022-04540-8

[11] A. Aldrees, H. Khan, A. Alzahrani, Applied Water Science 13, 156 (2023); https://doi.org/10.1007/s13201-023-01938-x

[12] Niranjan Patra, Gudiguntla Ravi, Chemistry select 9 (18), (2024).

[13] M. Dhonde, K. Sahu, V.S.S. Murty, Solar Energy 220, 418 (2021); https://doi.org/10.1016/j.solener.2021.03.072

[14] K. Prajapat, U. Mahajan, M. Dhonde, K. Sahu, P.M. Shirage, Chemical Physics Impact 8, 100607 (2024); https://doi.org/10.1016/j.chphi.2024.100607

[15] K. Sahu, M., Dhonde, V.S.S. Murty, Solar Energy 173, 551 (2018); https://doi.org/10.1016/j.solener.2018.07.091

[16] A. Gupta, K. Sahu, M. Dhonde, V.S.S. Murty, Energy 203, 296 (2020); https://doi.org/10.1016/j.solener.2020.04.043

[17] M. Dhonde, K.Sahu Dhonde, K. Purohit, V.V.S. Murty, Indian Journal of Physics and Proceedings of the Indian Association for the Cultivation of Science 93(1), 27 (2019); https://doi.org/10.1007/s12648-018-1275-4

[18] A.A. Jacob, L. Balakrishnan, S.R. Meher, K. Shambavi, Z.C. Alex, Journal of Alloys and Compounds 695, 3753 (2017); https://doi.org/10.1016/j.jallcom.2016.11.265

[19] I. Maryam, T. Iqbal, S. Afsheen, Atif Ali Journal of Inorganic and Organometallic Polymers and Materials 33(11), 3454 (2023); https://doi.org/10.1007/s10904-023-02776-9

[20] E. Ouadah, N.E. Hamdadou, A. Ammari, Journal of Electronic Materials 51(1), 356 (2022); https://doi.org/10.1007/s11664-021-09300-0

[21] M.M. Thwala, L.N. Dlamini, Environmental Technology 41(7), 2277 (2019); https://doi.org/10.1080/09593330.2019.1629635

[22] G. Akash, R. Shweta, M.M. Malik, Optik 242, 167266 (2021); https://doi.org/10.1016/j.ijleo.2021.167266

[23] N. Prabhu, S. Agilan, N. Muthukumarasamy, T.S. Sentil, International Journal of Chemistry Technology Research 6(7), 3487 (2014).

[24] S. Kalaiarasi, H. Kohila Subathra Christy, R. R. Muthuchudarkodi, C. Stella, Journal of Advanced Scientific Research 11 (4), 155 (2020).

[25] A. Jerold, R. Chellappa, R. Biju bennie, R, S. Mary Jelastin Kala, Ruby Jemima, Material Science: Material Electronics 34, 761(2023).

[26] B. Liu, D. Cai, D. Wang, L.Wang, Y.Wang, H. Li, Sensors and Actuators. B, Chemical 193, 28 (2014); https://doi.org/10.1016/j.snb.2013.11.057

[27] A. Hamidreza, S.T. Fatemeh, A. Maryam, Materials Research Express 6(10), 105024 (2019).

[28] S. Zhuiykov, E. Kats, Nanoscale Research Letters 9(1), 401(2014); https://doi.org/10.1186/1556-276X-9-401

[29] E. Spagnoli, S. Krik, B. Fabbri, M. Valt, M. Ardit, A. Gaiardo, L. Vanzetti, M. Della Ciana, V. Cristino, G. Vola, S. Caramori, C. Malagù, V. Guidi, Sensors and Actuators. B, Chemical 347, 130593(2021); https://doi.org/10.1016/j.snb.2021.130593

[30] Rishabh Sharma, Manika Khanuja, Shailesh Narayan Sharma, Om Prakash Sinha, International Journal of Hydrogen Energy 42(32), 20638 (2017); https://doi.org/10.1016/j.ijhydene.2017.07.011

[31] A. Popescu, I.V. Tudose, C. Romanitan, M.C. Popescu, M.Manica, Nanomaterials 14(14), 1227(2024); https://doi.org/10.3390/nano14141227

[32] T. Thilagavathi, D. Venugopal, R. Marnadu, J. Chandrasekaran, D. Thangaraju, Baskaran Palanivel, Mohamed S. Hamdy, M. Shkir, H. Elhosiny Ali, Journal of Physics and Chemistry of Solids 154,110066 (2021); https://doi.org/10.1016/j.jpcs.2021.110066

[33] H.D. Cho, I. Yoon, K.B. Chung, D.Y. Kim, T.W. Kang, Sh U. Yuldashev, Journal of Luminescence 195, 344 (2018); https://doi.org/10.1016/j.jlumin.2017.11.053

[34] S. Ramkumar, G. Rajarajan, Journal of Materials Science Materials in Electronics 27(11), 12185 (2016); https://doi.org/10.1007/s10854-016-5373-9

[35] Ran Ji, Ding Zheng, Chang Zhou, Lu Li., Materials 10(7), 820 (2017); https://doi.org/10.3390/ma10070820

[36] A.A. Jacob, L. Balakrishnan., Journal of Alloys and Compounds 949,169755 (2023); https://doi.org/10.1016/j.jallcom.2023.169755

[37] Saranya Subramanian, Balakrishnan Lakshmi Narayanan, Sangeetha Dhakshanamurthy, Lakshmi priya Selvaraj, Revista Materia 29(4), (2024). https://doi.org/10.1590/1517-7076-rmat-2024-0427